exoALMA. X. Channel maps reveal complex ^12CO abundance distributions and a variety of kinematic structures with evidence for embedded planets

Pinte, C.; Ilee, J.D.; Huang, J.; Benisty, M.; Facchini, S.; Fukagawa, M.; ... ; Zawadzki, B.

Citation

Pinte, C., Ilee, J. D., Huang, J., Benisty, M., Facchini, S., Fukagawa, M., ... Zawadzki, B. (2025). exoALMA. X. Channel maps reveal complex ^12CO abundance distributions and a variety of kinematic structures with evidence for embedded planets. *Astrophysical Journal Letters*, *984*(1). doi:10.3847/2041-8213/adc433

The Astrophysical Journal Letters, 984:L15 (13pp), 2025 May 1 https://doi.org/10.3847/2041-8213/adc433

exoALMA. X. Channel Maps Reveal Complex ^{12}CO Abundance Distributions and a Variety of Kinematic Structures with Evidence for Embedded Planets

Christophe Pinte[1,2], John D. Ilee[3], Jane Huang[4], Myriam Benisty[1,5], Stefano Facchini[6], Misato Fukagawa[7], Richard Teague[8], Jaehan Bae[9], Marcelo Barraza-Alfaro[8], Gianni Cataldi[10], Nicolás Cuello[1], Pietro Curone[6,11], Ian Czekala[12], Daniele Fasano[1,5], Mario Flock[13], Maria Galloway-Sprietsma[9], Himanshi Garg[2], Cassandra Hall[14,15,16], Iain Hammond[2], Caitlyn Hardiman[2], Thomas Hilder[2], Andrés F. Izquierdo[9,17,18,28], Kazuhiro Kanagawa[19], Geoffroy Lesur[1], Giuseppe Lodato[6], Cristiano Longarini[6,20], Ryan A. Loomis[21], Frédéric Masset[22], Francois Menard[1], Ryuta Orihara[19], Daniel J. Price[2], Giovanni Rosotti[6], Jochen Stadler[1,5], Hsi-Wei Yen[23], Gaylor Wafflard-Fernandez[1], David J. Wilner[24], Andrew J. Winter[5,13], Lisa Wölfer[8], Tomohiro C. Yoshida[10,25], and Brianna Zawadzki[26,27]

[1] Univ. Grenoble Alpes, CNRS, IPAG, 38000 Grenoble, France; christophe.pinte@univ-grenoble-alpes.fr
[2] School of Physics and Astronomy, Monash University, Clayton VIC 3800, Australia
[3] School of Physics and Astronomy, University of Leeds, Leeds LS2 9JT, UK
[4] Department of Astronomy, Columbia University, 538 W. 120th Street, Pupin Hall, New York, NY, USA
[5] Université Côte d'Azur, Observatoire de la Côte d'Azur, CNRS, Laboratoire Lagrange, 06304 Nice, France
[6] Dipartimento di Fisica, Università degli Studi di Milano, Via Celoria 16, 20133 Milano, Italy
[7] National Astronomical Observatory of Japan, Osawa 2-21-1, Mitaka, Tokyo 181-8588, Japan
[8] Department of Earth, Atmospheric, and Planetary Sciences, Massachusetts Institute of Technology, Cambridge, MA 02139, USA
[9] Department of Astronomy, University of Florida, Gainesville, FL 32611, USA
[10] National Astronomical Observatory of Japan, 2-21-1 Osawa, Mitaka, Tokyo 181-8588, Japan
[11] Departamento de Astronomía, Universidad de Chile, Camino El Observatorio 1515, Las Condes, Santiago, Chile
[12] School of Physics & Astronomy, University of St. Andrews, North Haugh, St. Andrews KY16 9SS, UK
[13] Max-Planck Institute for Astronomy (MPIA), Königstuhl 17, 69117 Heidelberg, Germany
[14] Department of Physics and Astronomy, The University of Georgia, Athens, GA 30602, USA
[15] Center for Simulational Physics, The University of Georgia, Athens, GA 30602, USA
[16] Institute for Artificial Intelligence, The University of Georgia, Athens, GA, 30602, USA
[17] Leiden Observatory, Leiden University, P.O. Box 9513, NL-2300 RA Leiden, The Netherlands
[18] European Southern Observatory, Karl-Schwarzschild-Str. 2, D-85748 Garching bei München, Germany
[19] College of Science, Ibaraki University, 2-1-1 Bunkyo, Mito, Ibaraki 310-8512, Japan
[20] Institute of Astronomy, University of Cambridge, Madingley Road, Cambridge CB3 0HA, UK
[21] National Radio Astronomy Observatory, 520 Edgemont Rd., Charlottesville, VA 22903, USA
[22] Instituto de Ciencias Físicas, Universidad Nacional Autónoma de México, Av. Universidad s/n, 62210 Cuernavaca, Mor., Mexico
[23] Academia Sinica Institute of Astronomy & Astrophysics, 11F of Astronomy-Mathematics Building, AS/NTU, No.1, Sec. 4, Roosevelt Rd, Taipei 10617, Taiwan
[24] Center for Astrophysics—Harvard & Smithsonian, Cambridge, MA 02138, USA
[25] Department of Astronomical Science, The Graduate University for Advanced Studies, SOKENDAI, 2-21-1 Osawa, Mitaka, Tokyo 181-8588, Japan
[26] Department of Astronomy, Van Vleck Observatory, Wesleyan University, 96 Foss Hill Drive, Middletown, CT 06459, USA
[27] Department of Astronomy & Astrophysics, 525 Davey Laboratory, The Pennsylvania State University, University Park, PA 16802, USA

Received 2024 November 14; revised 2025 March 17; accepted 2025 March 19; published 2025 April 28

Abstract

We analyze the ^{12}CO $J = 3$–2 data cubes of the disks in the exoALMA program. 13/15 disks reveal a variety of kinematic substructures in individual channels: large-scale arcs or spiral arms, localized velocity kinks, and/or multiple faints arcs that appear like filamentary structures on the disk surface. We find kinematic signatures that are consistent with planet wakes in six disks: AA Tau, SY Cha, J1842, J1615, LkCa 15, and HD 143006. Comparison with hydrodynamical and radiative transfer simulations suggests planets with orbital radii between 80 and 310 au and masses between 1 and 5 $M_{\rm Jup}$. Additional kinematic substructures limit our ability to place tight constraints on the planet masses. When the inclination is favorable to separate the upper and lower surfaces (near 45°, i.e., in 7/15 disks), we always detect the vertical CO snowline and find that the ^{12}CO freeze-out is partial in the disk midplane, with a depletion factor of $\approx 10^{-3}$–10^{-2} compared to the warm molecular layer. In these same seven disks, we also systematically detect evidence of CO desorption in the outer regions.

Unified Astronomy Thesaurus concepts: Protoplanetary disks (1300); Exoplanet formation (492); Radiative transfer (1335); Hydrodynamics (1963); Planetary-disk interactions (2204); Exoplanets (498); Submillimeter astronomy (1647)

1. Introduction

The remarkable sensitivity of the exoALMA Large Program (R. Teague et al. 2025) enables us to map molecular line emission from protoplanetary disks with unprecedented detail. With a velocity resolution of ≈ 26 m s^{-1} and spatial resolution of $\approx 0\farcs1$, we can explore the intricate distribution of gas and its dynamics, which are critical for understanding the physical

---

[28] NASA Hubble Fellowship Program Sagan Fellow.

Table 1
Main Kinematic Substructures in the exoALMA Sources

Source	$v_{\rm syst}$ (km s^{-1})	Beam (arcsec)	Δv (km s^{-1})	Peak $T_{\rm b}$ (K)	$T_{\rm b}$ Sensitivity[a] (K)	Kinematic Deviations
MWC 758	5.86	0.12	100	95	4.5	Large-scale arcs
HD 135344B	7.07	0.11	100	114	3.4	Large-scale arcs + velocity kink
CQ Tau	6.20	0.12	200	91	1.7	Large-scale arcs + velocity kink
J1604	4.60	0.15	100	84	1.5	Large-scale arcs
AA Tau	6.50	0.15	100	73	1.7	Velocity kink
SY Cha	4.10	0.15	100	56	1.6	Velocity kink + filaments
J1842	5.93	0.15	100	64	1.5	Velocity kink
J1615	4.75	0.15	100	56	1.3	Velocity kink + filaments
LkCa 15	6.29	0.15	100	57	1.2	Velocity kink + filaments
HD 143006	7.70	0.10	100	78	4.9	Velocity kink
J1852	5.46	0.12	100	82	2.7	Filaments
DM Tau	6.03	0.20	100	56	1.1	Filaments + velocity kink
HD 34282	−2.30	0.11	100	93	2.2	Filaments
V4046 Sgr	2.90	0.12	100	98	2.3	Smooth
PDS 66	3.96	0.15	100	81	1.8	Smooth

Note. The spatial and spectral resolutions with their corresponding peak brightness temperatures and sensitivity are indicated for the cubes used in Figures 1–5.

[a] We used the Rayleigh–Jeans approximation for sensitivity to maintain consistency with the ALMA observing tool, while the full blackbody function was used for all other brightness temperatures.

processes at play during planet formation (C. Pinte et al. 2023a). Previous Letters in this series primarily focused on integrated (moment and/or peak) maps and azimuthally averaged velocity curves to search for non-Keplerian motions, pressure gradients, or nonthermal broadening (T. Hilder et al. 2025; A. F. Izquierdo et al. 2025; J. Stadler et al. 2025; C. T. Yoshida et al. 2025).

In this Letter, we extend the analysis to individual channel maps, which provide a complementary approach by isolating specific velocity channels across the emission line profiles. This allows us to search for subtle kinematic structures that could be overlooked when examining spectrally concatenated data, to resolve both the upper and lower molecular emission surfaces, and to search for diffuse and faint emission. Such emission may trace complex chemical processes, such as the freeze-out of volatile molecules onto dust grains, and photodissociation and photodesorption driven by ultraviolet light, offering insight into the disk's thermal structure and chemistry. These processes can alter the chemical makeup of the disk, influencing the composition of material that eventually forms planets (K. I. Öberg et al. 2023).

We classify the 15 exoALMA disks based on their kinematic substructures, identifying distinct patterns that suggest various underlying physical processes. For disks exhibiting signatures consistent with the presence of embedded planets, we perform hydrodynamical and radiative transfer simulations, with the goal of estimating the mass of the potential planets.

2. Observations and Imaging

We inspected the ^{12}CO $J = 3$–2 exoALMA data cubes at various spatial ($0\farcs1$–$0\farcs3$) and spectral (28–200 m s^{-1}) resolutions to systematically search for kinematic substructures. In most cases, we also reimaged the visibilities using the standard exoALMA imaging procedure (R. Loomis et al. 2025), but with additional weighting schemes and spectral binning, in order to tailor the spatial resolution and signal-to-noise ratio, and ascertain the robustness of the detected kinematic structures (Table 1). Continuum subtraction may impact the measured brightness temperature and apparent morphology of optically thick line emission (Y. Boehler et al. 2017). To ensure that the kinematic structures are not artificially created by continuum subtraction, we imaged all the channel maps without continuum subtraction, and checked that the detected kinematic deviations are also present in the corresponding continuum-subtracted maps. The disks with the most interesting structures were also reimaged using regularized maximum likelihood imaging instead of CLEAN (B. Zawadzki et al. 2025), confirming that the detections presented here are not artifacts of the imaging process.

We focus in this letter on the ^{12}CO data cubes, but also note that the ^{13}CO cubes show counterparts of the kinematic substructures presented here, while the limited signal-to-noise ratio of CS cubes makes it difficult to robustly detect any velocity deviation.

3. Results

3.1. A Variety of Kinematic Substructures

We visually detect velocity deviations in ^{12}CO channel maps in 13 of the 15 exoALMA objects. Figures 1–4 show representative channel maps of the ^{12}CO emission for all disks, classified according to the dominant type of kinematic structures: (i) large-scale kinematic deviations over most of the velocity range, (ii) a primary velocity kink suggesting at least one embedded planet, (iii) multiple faints arcs that appear like a filamentary structure on the disk surface, and (iv) smooth disks with no obvious kinematic structures. The detected kinematic substructures are summarized in Table 1.

To help visualize the velocity deviations, we overlay the expected locations of the isovelocity curves on the upper surface, assuming the disks are in Keplerian rotation. We used the code dynamite (C. Pinte et al. 2018a) to extract the disk's geometric parameters (outer radius, inclination, position angle (PA), systemic velocity, and stellar masses) and the altitude of the CO emission layer. Parameters are summarized in Table 2. We verified that all those parameters are consistent with the values derived with discminer by A. F. Izquierdo et al. (2025)

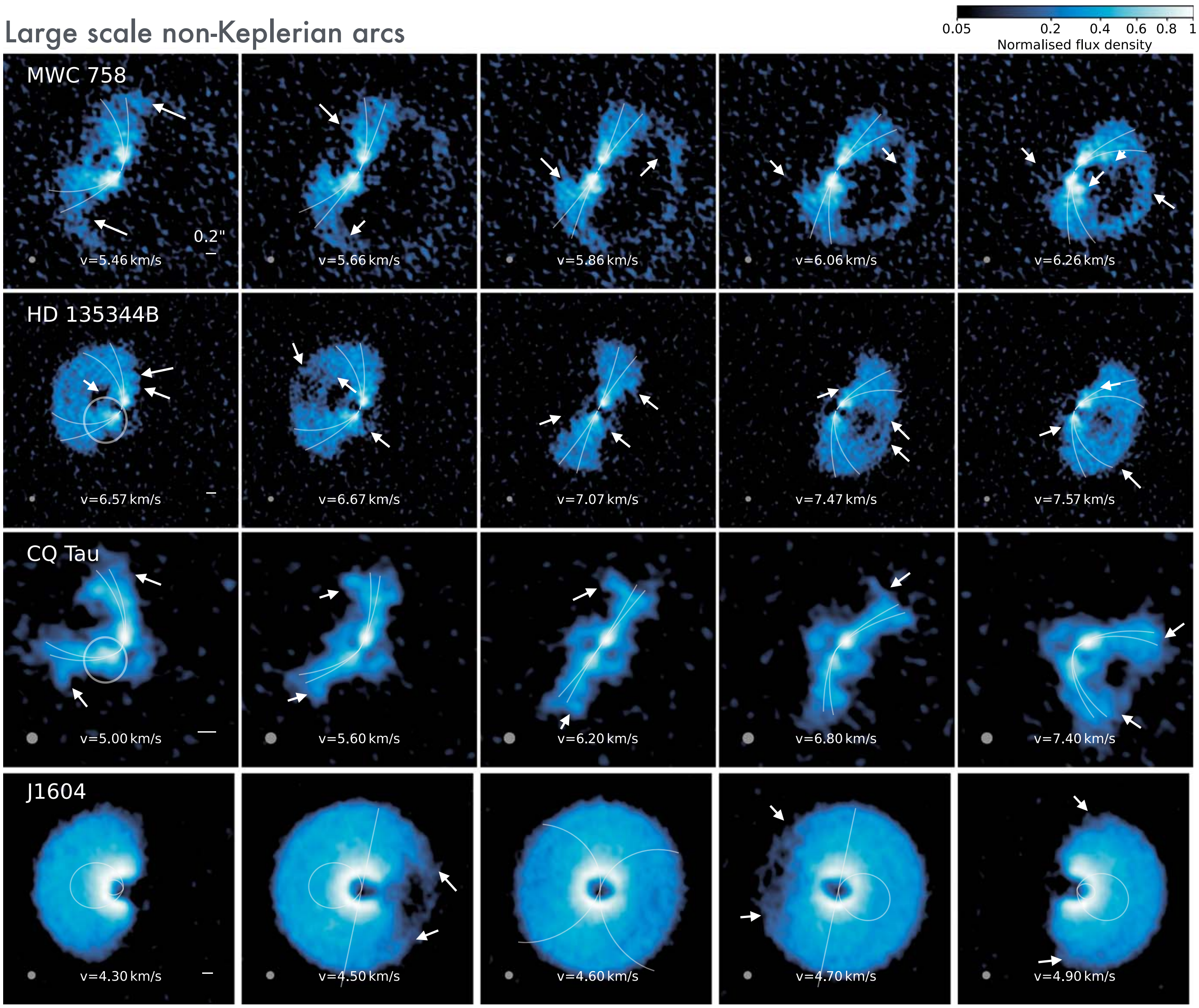

Figure 1. Sources displaying large-scale non-Keplerian arcs. For each object, we show the channel at systemic velocity (central column), as well as channels at two velocity offsets on the blue side of the line (first two columns) and the opposite channels on the red side of the line (last two columns). Solid lines indicate the expected location of the isovelocity curves at Keplerian velocities ±100 m s^{-1}. White arrows indicate deviations from the expected isovelocity curves for Keplerian rotation, and white circles highlight velocity kinks, i.e., distortions of the isovelocity curves. The beam is indicated as a gray circle and the horizontal white line is a 0.″2 scale. The color map traces the square root of the intensity between zero and the peak. Note that the ringlike structure seen in CQ Tau is the continuum emission.

and that the emission surfaces closely match those derived and discussed in detail by M. Galloway-Sprietsma et al. (2025).

Figure 1 shows sources with large-scale kinematic deviations, in the form of extended arcs or spirals, that span most of the velocity range. Deviations are dominated by a major structure near the outer edge of the detected ^{12}CO emission in CQ Tau and J1604, while MWC 758 and HD 135344B also show multiple arcs at all radii, reminiscent of structures seen, for instance, in HD 142527 (H. Garg et al. 2021) and HD 100546 (B. J. Norfolk et al. 2022). Interestingly, CQ Tau also displays a "velocity kink" located on top of the continuum ring (left panel at $v = 5\ \mathrm{km\ s^{-1}}$), similar to the one detected in HD 100546 (B. J. Norfolk et al. 2022), which appears as a Doppler flip in the peak velocity residual maps (S. Casassus & S. Pérez 2019). A large velocity kink is also detected in HD 135344B at ≈6.6 km s^{-1}, and corresponds to the Doppler flip discussed by A. F. Izquierdo et al. (2025). The large velocity deviations observed in MWC 758, HD 135344B, and CQ Tau are reminiscent of the predicted kinematic signatures from massive (above the planetary regime) companions on misaligned orbits (e.g., D. J. Price et al. 2018; J. Calcino et al. 2023, 2024; E. Ragusa et al. 2024). This would be consistent with the extended spiral arms seen in scattered light in these sources (T. Muto et al. 2012; M. Benisty et al. 2015; I. Hammond et al. 2022). MWC 758's outer arc shows a remarkable redshifted emission structure with a velocity shift larger than the expected Keplerian velocity at this location, suggesting a structure not associated with the disk rotation. This may trace a wind or the remains of a past interaction with a cloud or a stellar flyby (N. Cuello et al. 2020). We note that M. Reggiani et al. (2018) found a point source at 2.″3, but concluded it is likely to be a background source. We also note that the high-velocity channels of J1604 (not shown here) present a significant change in PA, i.e., a warp, as previously observed by J. Stadler et al. (2023), which suggested the

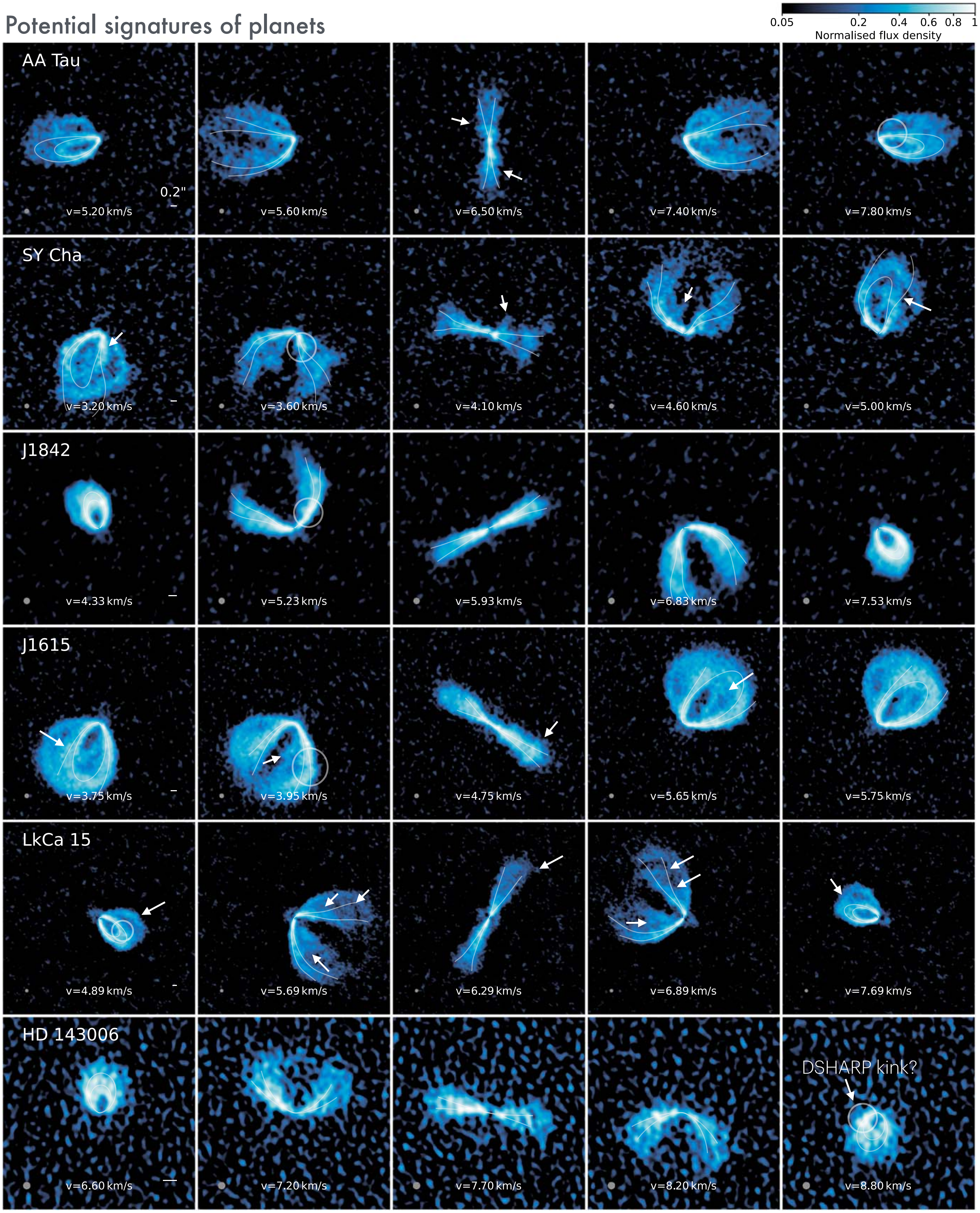

Figure 2. Sources with velocity kinks consistent with embedded planets (white circles). White arrows indicate additional deviations from Keplerian rotation. Beams and scales as in Figure 1.

presence of a planet inside the inner cavity (see also Figure 6 of R. Teague et al. 2025). The almost face-on orientation of J1604 suggests that the arc seen in most channels is primarily dominated by vertical motions, which is reminiscent of buoyancy spirals (e.g., J. Bae et al. 2021), and may indicate the presence of an embedded planet.

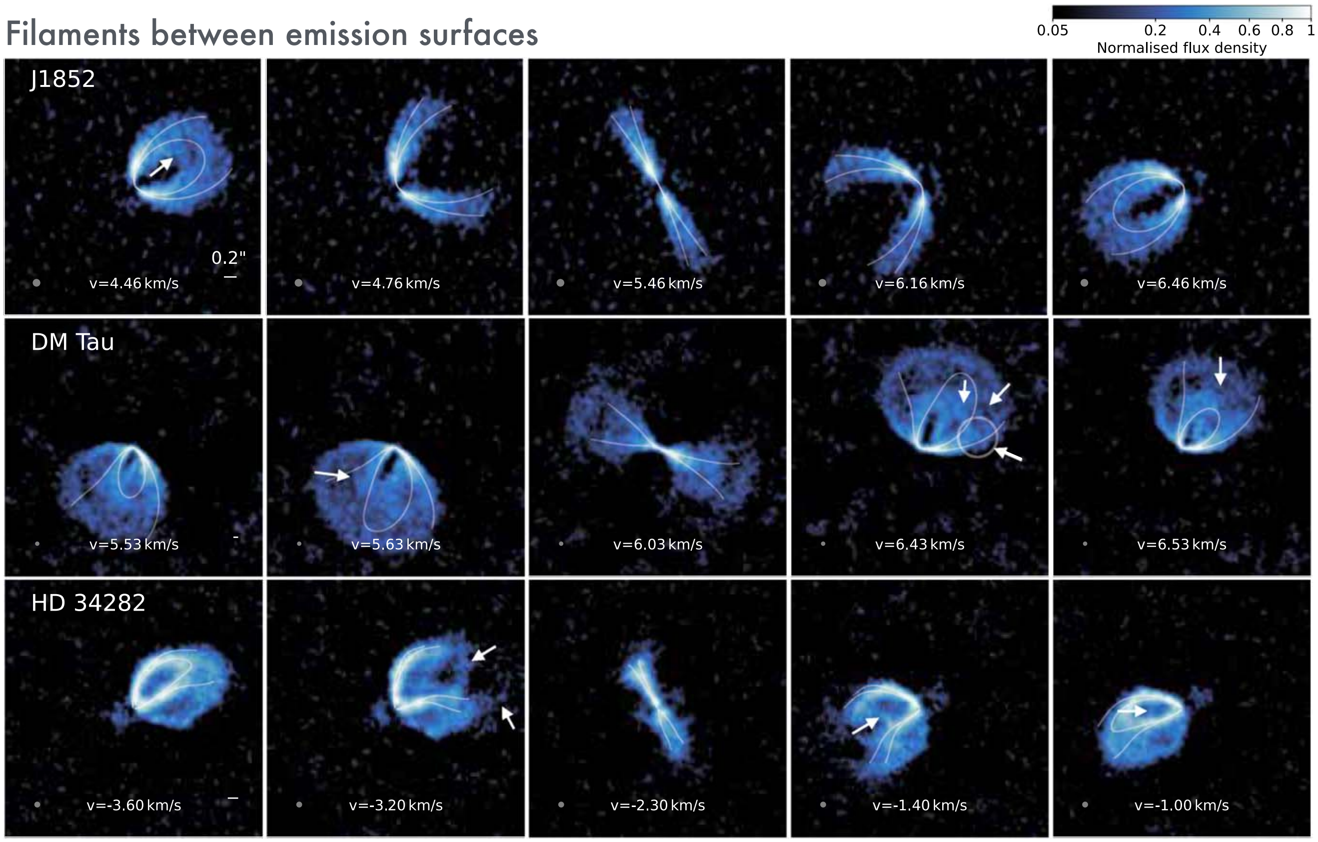

Figure 3. Sources showing a filamentary pattern between the emission surfaces (indicated by white arrows). Note that such patterns are also visible in SY Cha, J1615, and LkCa 15, as shown in Figure 2. A potential kink in the isovelocity is shown with a white circle. Beams and scales as in Figure 1.

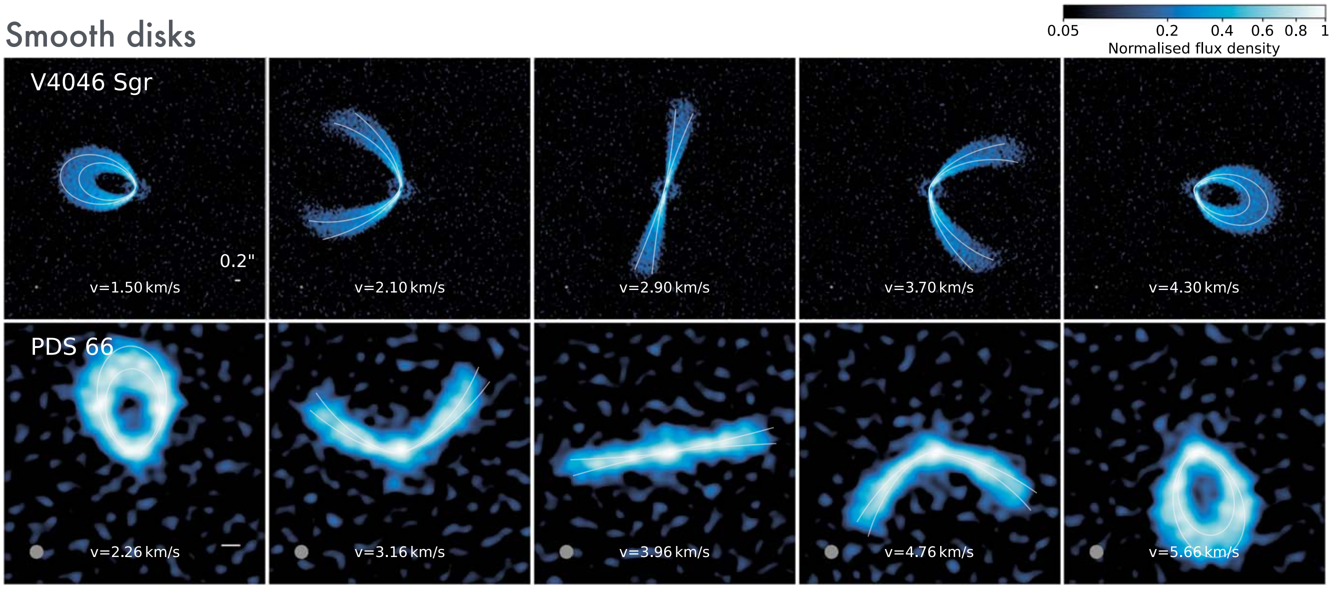

Figure 4. Sources with smooth, Keplerian-looking, velocity structure, or with signal-to-noise ratio too low to extract reliable structures at the considered scales. Beams and scales as in Figure 1.

Figure 2 shows sources with velocity "kinks" that may indicate the wake of embedded planets. In each panel, the white circle highlights the velocity kink near the planet candidate, but most sources also display additional deviations from Keplerian rotation, as indicated by the white arrows. The most prominent kink is detected in SY Cha at 3.6 km s^{-1}, but additional structures are also detected at different velocities in that source. Isolating a main kink is more difficult for AA Tau, J1842, J1615, and LkCa 15, as multiple kinks are detected across several channels. This seemingly argues against a planetary

Table 2
Parameters Used in the Phantom + mcfost Modeling

Source	M_* ($M_\odot$)	$M_{\rm disk}$ ($M_\odot$)	i (deg)	PA (deg)	$r_{\rm out}$ (au)	$r_{\rm c}$ (au)	$r_{\rm planet}$ (au)	**Estimate of Planet Mass** ($M_{\rm Jup}$)
AA Tau	0.8	5×10^{-3}	120	272	240	100	80	2
J1615	1.15	5×10^{-3}	133	325.5	435	250	310	2
J1842	1.1	5×10^{-3}	38	207	220	100	105	1
LkCa 15	1.15	10^{-2}	50	62	650	300	240	5
SY Cha	0.8	10^{-2}	52	348	310	150	140	5

Note. Stellar masses and disk geometry were derived with dynamite. The planet masses were estimated by comparing the ^{12}CO synthetic cubes to the data (Figure 7).

origin, as previous studies have suggested that an embedded planet would generate only localized velocity perturbations (C. Pinte et al. 2018b, 2019). However, it was later shown that a kink is created each time the planet wake crosses an isovelocity curve (F. Bollati et al. 2021), as observed in HD 163296 (J. Calcino et al. 2022) and suggested in IM Lupi (H. J. Verrios et al. 2022, but we note that G. Lodato et al. 2023 proposed gravitational instability (GI) as an alternative explanation for the spiral structure). The detected velocity kinks indeed appear to be connected to large substructures seen in the peak intensity maps, as illustrated in Figure 5. In particular, the locations of the velocity kinks align with dips in the peak brightness map for LkCa 15, SY Cha, and J1615. We detect a kink in HD 143006 at 8.8 km s^{-1}, at the same location and velocity as the one detected in the DSHARP data in band 6 (L. M. Pérez et al. 2018; C. Pinte et al. 2020). This potential kink is only visible in cubes imaged at a spatial resolution of 0.″1. This is the maximum resolution attainable with our baselines, and, as a result, the limited signal-to-noise ratio makes it difficult to fully confirm the DSHARP detection. We investigate in Section 4 whether the observed structures might be due to planets.

Figure 3 presents sources showing filamentary structures between the main isovelocity curves, either in the form of multiple arcs in the upper emission layer (J1852 and HD 34282) or between the upper and lower surfaces in the case of DM Tau. SY Cha, J1615, and LkCa 15 (in Figure 2) also show some evidence of filaments between their upper and lower emission surfaces. These structures may trace spiral arms running through the disk surface. The filamentary structure in DM Tau is detected in most channels, but is most obvious around 6.4 km s^{-1}, where we also detect a tentative kink in the isovelocity curve, which appears connected to the filaments.

Finally, Figure 4 shows sources for which we did not detect any obvious structure in the channel maps, either because the emission is smooth and appears to follow an almost Keplerian rotation profile for V4046 Sgr or because the small disk size makes it difficult to confidently detect substructures for PDS 66. The smooth velocity field, in particular compared to other exoALMA sources, is surprising as V4046 Sgr is a known spectroscopic binary (P. B. Byrne 1986; H. C. Stempels & G. F. Gahm 2004), with known substructures in scattered light and millimeter continuum emission (H. Avenhaus et al. 2018; R. Martinez-Brunner et al. 2022).

Our classification is subjective, and some sources clearly exhibit multiple types of substructures. This classification is also biased by inclination, where sources near 45° offer the best orientation to detect small velocity perturbations that may be caused by planets or emission between the upper and lower layers, while sources closer to pole-on are more favorable for detecting vertical motions.

The structures we detect in channel maps mostly correspond to those observed in integrated or peak intensity and velocity maps as presented by A. F. Izquierdo et al. (2025). A comparison with these integrated maps reveals that some of the kinematic deviations we see in channels are part of larger-scale kinematic structures, such as spirals, for instance in the disks of MWC 758, HD 135344B, and CQ Tau.

3.2. CO Vertical Snowlines and Desorption

The channel maps also reveal a complex distribution of CO abundance within the disks, especially in those at intermediate inclinations, where projection effects between the upper and lower emitting surfaces are limited, allowing for a clearer view of the spatial distribution of the molecular emission.

First, we observe a clear separation between the upper and lower CO surfaces, highlighting the stratified structure of the emission, as has been seen in many disks already (I. de Gregorio-Monsalvo et al. 2013; K. A. Rosenfeld et al. 2013; C. Pinte et al. 2018a; C. J. Law et al. 2021, 2022; R. Teague et al. 2021; T. Paneque-Carreño et al. 2023). For a detailed extraction and discussion of the emission surfaces in the exoALMA sample, we refer to M. Galloway-Sprietsma et al. (2025).

Second, in every disk where we can clearly separate the upper and lower surfaces, we consistently detect nonzero emission between these surfaces. Figure 6 shows channels of HD 34282, DM Tau, LkCa 15, J1615, SY Cha, AA Tau, and J1842 with a larger beam size of 0.″25 to enhance fainter emission. In the central two columns, the regions between the upper and lower surfaces are indicated with orange arrows. These regions are always brighter than the areas between the near and far sides of the upper surface, indicated by red arrows. We selected channels where the projected separation between the various isovelocity curves is similar, ruling out beam effects as the cause of this difference. This confirms that the emission between the upper and lower surfaces is real, indicating that CO is not fully frozen out onto dust grains in the disk midplane, and suggesting some degree of desorption. We note that the majority of disks exhibiting evidence of desorption also show potential signs of planets. This is likely a coincidence, resulting from favorable inclinations that allow for a clear separation of the upper and lower surfaces, in turn enabling the detection of both midplane emission and velocity kinks on the emission surfaces.

Finally, at large radii, we detect diffuse emission where the upper and lower surfaces appear to merge (white arrows in the

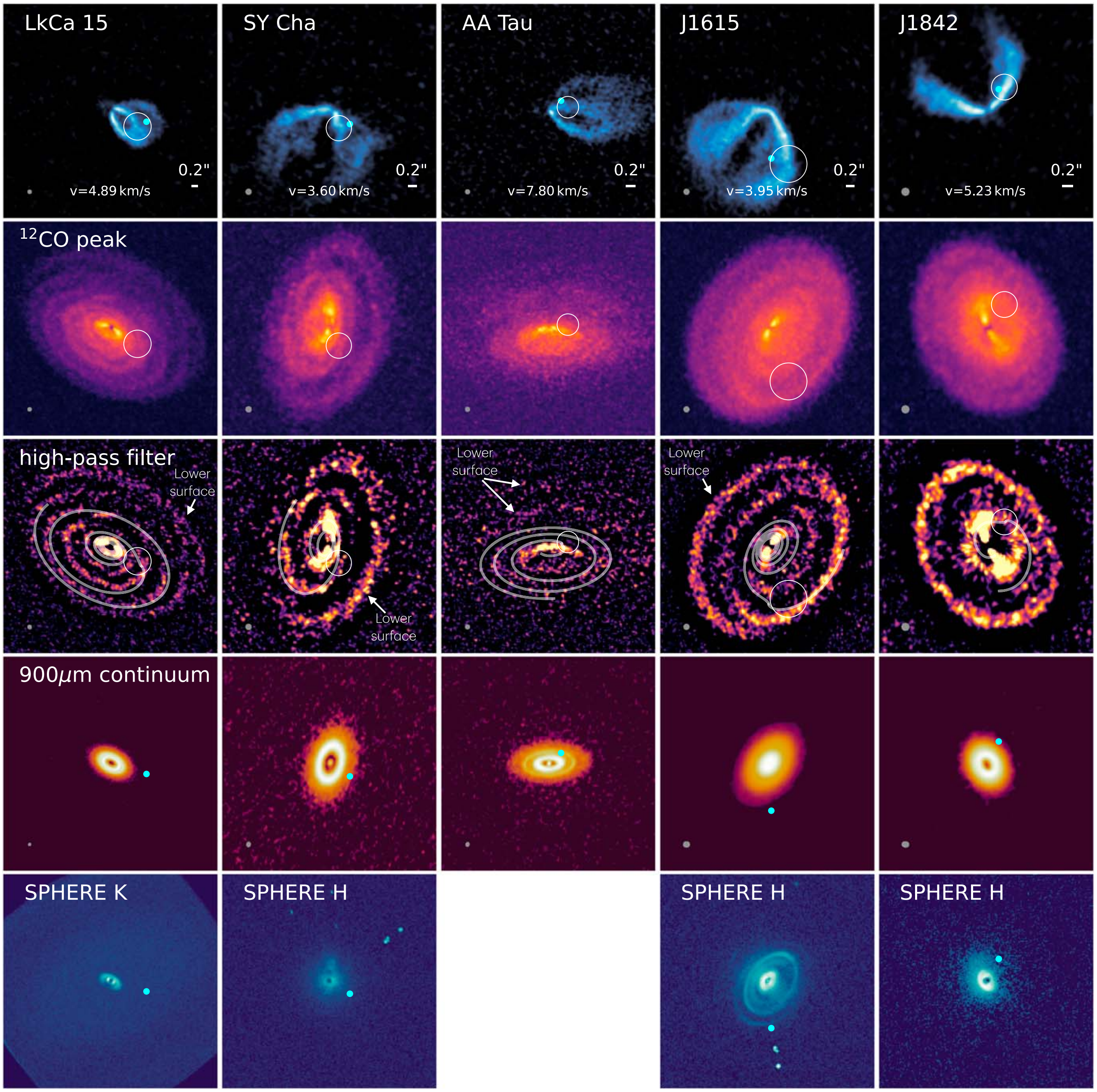

Figure 5. ^{12}CO $J = 3$–2 observations from the Atacama Large Millimeter/submillimeter Array (ALMA), continuum emission, and near-infrared scattered light images for the five newly detected planet candidates. The first row shows the ^{12}CO $J = 3$–2 channels with the identified velocity kinks. The second row presents the corresponding peak intensity map. The third row displays a high-pass filtered peak intensity map using a Gaussian kernel twice the size of the beam, where we overlay the location of the planetary wake, derived using the same thermal structure as in the phantom models and projected vertically onto the CO-emitting surface. The fourth row shows the exoALMA continuum (P. Curone et al. 2025), and the last row presents SPHERE dual-beam polarimetric imaging observations. The white circles indicate the velocity kinks shown in Figure 2, while the blue dot marks the deprojected location on the disk midplane. No SPHERE data are available for AA Tau, as it is currently too faint to lock the adaptive optics system.

first and last columns of Figure 6). This diffuse emission is also detected when extracting the emission surfaces (M. Galloway-Sprietsma et al. 2025). This implies that CO remains in the gaseous phase throughout the disk's vertical extent at these distances, likely due to photodesorption by UV radiation (either from the central star via scattering or due to external illumination). This partial CO freeze-out in the midplane and desorption in the outer regions was also observed in IM Lupi (C. Pinte et al. 2018a).

4. A Planetary Origin ?

4.1. Modeling

To determine whether embedded planets explain the observed velocity kinks in Figure 2, we performed a series of hydrodynamical and radiative transfer simulations for AA Tau, LkCa 15, SY Cha, J1615, and J1842. We note that G. Ballabio et al. (2021) already modeled HD 143006. Our aim is not to develop a detailed model for each source; instead, we test,

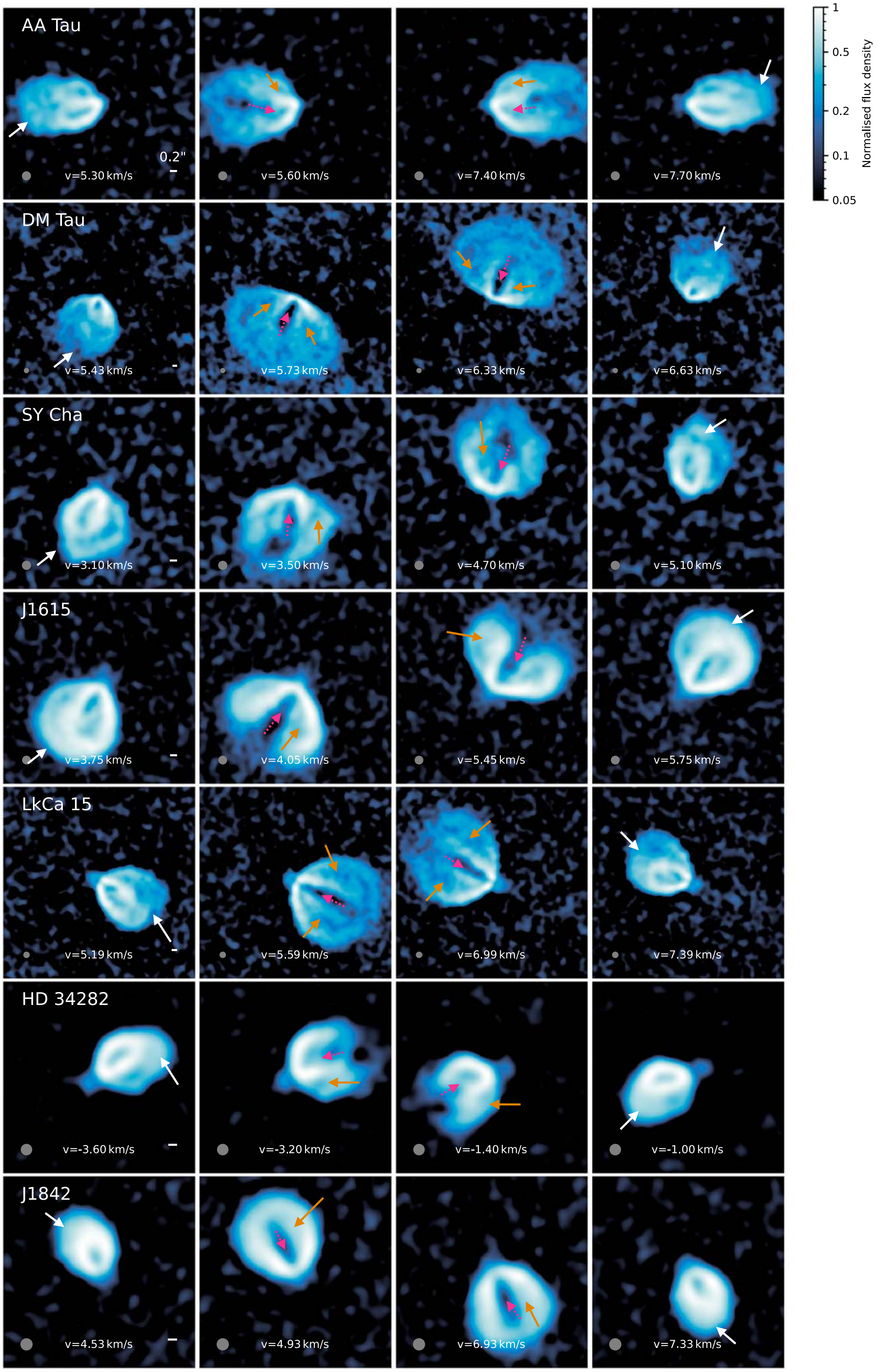

Figure 6. Evidence for complex CO abundance distributions. The white arrows in the first and last columns show regions where the upper and lower surfaces merge, indicating desorption. In the central two columns, the orange arrows show that the emission between the upper and lower surfaces is always greater than the emission between the near and far sides of the upper isovelocity curves (red arrows with dotted line), even if the projected separation is similar. The beam is 0.″25. The color map represents the log of the intensity to highlight low-brightness regions.

through a restricted exploration of the parameter space, whether a single planet can reasonably explain the observed channel maps. In particular, we focus on the ^{12}CO channel maps and do not attempt to model all observables, such as submillimeter continuum images or scattered light images.

We model each object as a disk surrounding a central star with one embedded planet. We used the stellar mass and geometrical parameters derived with dynamite (Table 2). We performed 3D gas-only simulations with the smoothed particle hydrodynamics (SPH) code phantom (D. J. Price et al. 2018). We used 10^6 particles and evolved the system for 20 planet orbits, which is sufficient to establish the flow pattern around the planet. Because the ^{12}CO emission arises from the disk's upper layers, which are poorly sampled by the SPH method (where the resolution follows the mass), we split each SPH particle into 13. We place 12 new particles on an icosahedron centered on the initial particle, at a radius equal to the smoothing length of the initial particle. Each new SPH particle has a mass of 1/13 of the initial particle mass and retains the initial particle's velocity. We evolve this higher-resolution simulation for an additional two planet orbits. To achieve a mean Shakura–Sunyaev viscosity of 5×10^{-3}, we set the shock viscosity to $\alpha_{\rm av} = 0.2$, which remains above the lower bound of $\alpha_{\rm av} \approx 0.1$ needed to resolve physical viscosity in phantom (D. J. Price et al. 2018). We set the inner radius to 5 au. We neglect self-gravity and use a disk mass of $5 \times 10^{-3}\,M_\odot$ for all disks, but note that we rescale the disk masses in mcfost to the values indicated in Table 2 to match the separation between emitting layers.

We set up the disks with a tapered surface density profile:

$$\Sigma(r) = \Sigma_c \left(\frac{r}{r_c}\right)^{-\gamma} \exp\left(-\left(\frac{r}{r_c}\right)^{2-\gamma}\right)$$

with $\gamma = 0.8$. We adopted a vertically isothermal equation of state with $H/R = 0.1$ at $r = 50$ au and a power-law index for the sound speed of $-1/3$.

For each object, we embedded a single planet at the projected location of the detected primary kinks with an initial mass of 1, 2, 5, or 10 $M_{\rm Jup}$, and with an accretion radius set to 0.125 times the Hill radius.

We postprocessed the models with the radiative transfer code mcfost (C. Pinte et al. 2006; C. Pinte et al. 2009) to compute the dust temperature structure and CO maps, matching Voronoi cells to SPH particles. The combination of phantom and mcfost was benchmarked and validated by J. Bae et al. (2025). We assumed 1 Myr isochrones to set the luminosities and effective temperatures of the star (L. Siess et al. 2000) and planets (F. Allard et al. 2012). As we do not see any evidence of local heating in the exoALMA data, we did not include any accretion luminosity, unlike C. Pinte et al. (2023b). We assumed astrosilicate grains (J. C. Weingartner & B. T. Draine 2001) with sizes following $\mathrm{d}n(a) \propto a^{-3.5}\mathrm{d}a$ between 0.03 and 1000 μm and a uniform gas-to-dust ratio of 100. We computed the dust optical properties using the Mie theory. The dust model is only used to set the disk thermal balance, where we assumed that $T_{\rm gas} = T_{\rm dust}$ and that the CO $J = 3$–2 transition is in local thermodynamic equilibrium. We set the turbulent velocity to zero, and only thermal broadening is contributing to the local line width.

We set the CO abundance following the prescription in Appendix B of C. Pinte et al. (2018a) to account for freeze-out, photodissociation, and photodesorption. In the warm molecular layer, we set the ^{12}CO abundance to 10^{-4} relative to H. Below 20 K, we deplete this abundance by a factor that we allow to vary, unless the UV field computed by mcfost is high enough for photodesorption to occur.

Phantom and mcfost models are available via Harvard Dataverse (C. Pinte 2025).

4.2. Comparison with Data

Figure 7 shows the predicted emission for our model grid. For each source, we compare the channel where the velocity kink is most visible to our synthetic models. In all cases, a 10 $M_{\rm Jup}$ planet produces velocity deviations that are larger than those observed. The detected velocity kinks are best reproduced with a planet mass of 2 $M_{\rm Jup}$ for LkCa 15, AA Tau, and J1615, 5 $M_{\rm Jup}$ for SY Cha, and 1 $M_{\rm Jup}$ for J1842.

The planet model matches the observations well for LkCa 15, J1615, and J1842, in terms of both shape and amplitude of the kink. In LkCa 15, additional planets are likely present at small separations, as discussed by C. Gardner et al. (2025), who imaged the disk at higher spatial resolution ($\lesssim 0\farcs05$) by combining exoALMA data with longer-baseline observations. In particular, C. Gardner et al. (2025) detected an additional velocity kink at the systemic velocity at a separation of $\lesssim 0\farcs1$, which is smeared out at our spatial resolution. The agreement between our synthetic maps and the observations is particularly remarkable for J1615, where our model also reproduces the velocity kink seen on the lower surface.

For SY Cha, a planet of approximately 5 $M_{\rm Jup}$ produces a velocity kink with the correct amplitude, but its shape is not as sharp as in the observations, suggesting that other physical processes might be at play. For AA Tau, the signal-to-noise ratio at the location of the velocity kink is low ($\approx$5), making it difficult to assess the model's ability to precisely predict the planet mass. Nevertheless, a 10 $M_{\rm Jup}$ planet can be ruled out, as it would open a deep gap that causes the emission along the isovelocity curve in the southern region to appear too narrow.

We do not attempt to precisely match the brightness of the emitting upper and lower surfaces or the midplane. However, we find that models with a depletion factor between 10^{-3} and 10^{-2} (i.e., an abundance of 10^{-7}–10^{-6} relative to H where the temperature is below 20 K) reproduce the emission significantly better than models assuming complete freeze-out or no freeze-out (Figure 8). We note that this range is only indicative, as we varied the freeze-out fraction for a single hydrodynamical model and did not explore potential correlations with, for instance, the disk density and thermal structures, the overall CO abundance, or the amount of UV radiation. Moreover, we did not aim to achieve a perfect match to the data. More quantitative constraints would require a dedicated fit to the data, as done, for instance, by C. Hardiman et al. (2025, in preparation) for DM Tau. Interestingly, the range we obtain is comparable to the depletion factor of $\approx 1/300$ derived by C. Qi & D. J. Wilner (2024) for HD 163296 by modeling the optically thin C^{17}O and C^{18}O $J = 1$–0 and $J = 2$–1 lines.

5. Discussion

The deep exoALMA observations provide an unprecedented view of the ^{12}CO distribution in protoplanetary disks. The channel maps show that CO only partially freezes out in the midplane, even when the temperature is below 20 K, and our

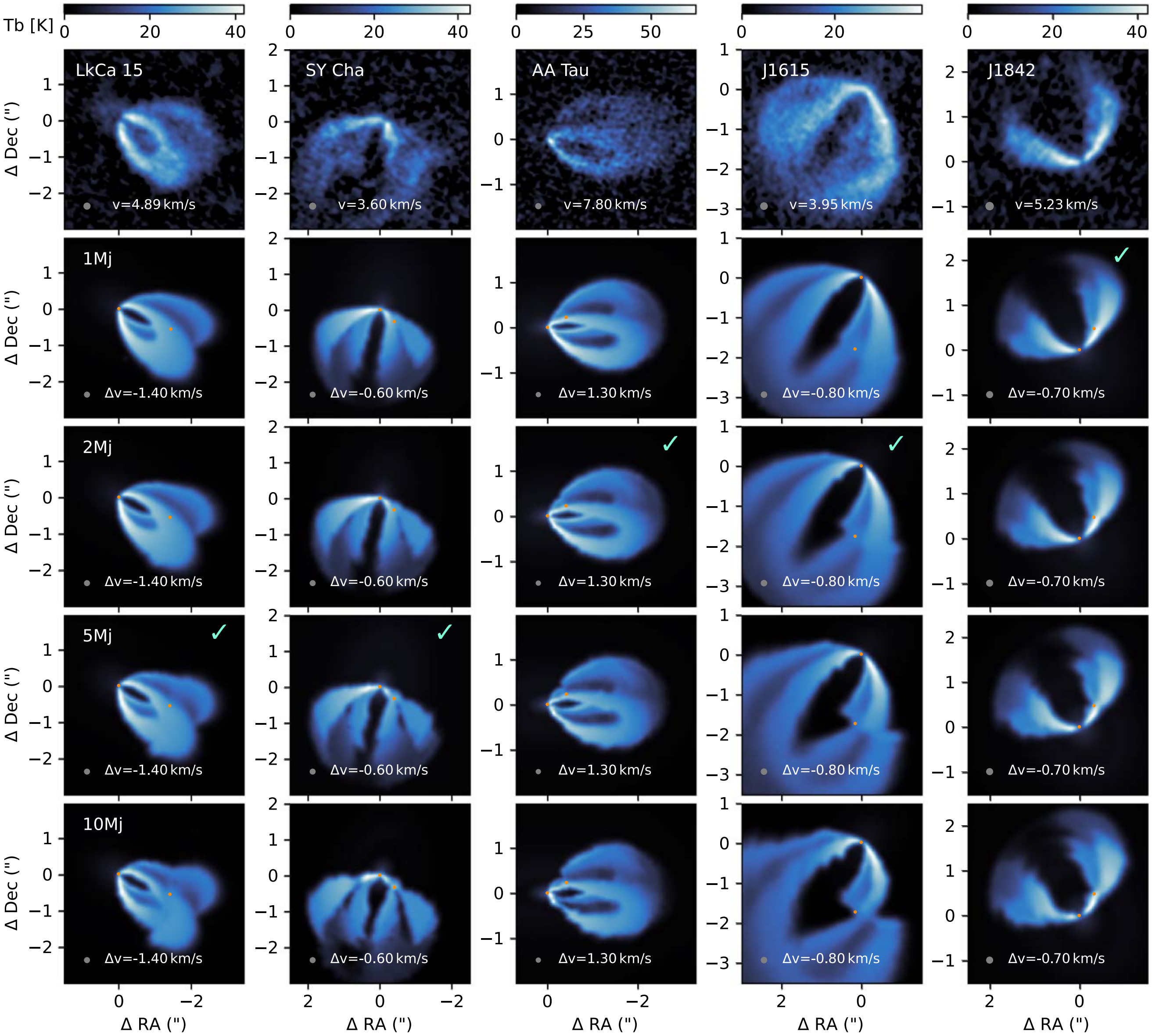

Figure 7. Comparison of ^{12}CO $J = 3$–2 ALMA observations (top row) with synthetic channel maps from our 3D hydrodynamics calculations with embedded planets of 1, 2, 3, and 5 $M_{\rm Jup}$ (from top to bottom). The channel width is 0.1 km s^{-1}. Synthetic maps were convolved to a Gaussian beam to match the spatial resolution of the observations. Orange dots show the location of the sink particles: central star and planet. The Δv value indicates the offset from systemic velocity. The green checkmark indicates the models that visually best reproduce the observations.

simple modeling suggests a relative abundance of the order of 10^{-3}–10^{-2} compared to the CO abundance in the emitting layers. The midplane abundance we derive is a bit higher than the value found by C. Pinte et al. (2018a) in IM Lupi (but that study was at a lower spatial resolution of ≈0.″4). Desorption at large radii is also systematically required to reproduce the channel maps. The inferred abundance from the observations is generally consistent with thermochemical models (e.g., P. Woitke et al. 2009; S. Bruderer et al. 2012), and more detailed comparisons with models offer a path to better understand photodesorption processes and the role of UV radiation in shaping the outer disk.

As highlighted by C. P. Dullemond et al. (2020), ^{12}CO emission from the midplane could potentially be used to directly measure the disk midplane temperature. This method was initially developed for the disk around the Herbig Ae star HD 163296, where most of the disk midplane is above 25 K, and thus CO is not frozen out, allowing the line to reach optical depths greater than unity. This is likely not the case for the T Tauri stars in our sample. Nevertheless, the systematic detection of midplane CO emission may offer a way to extend the mapping of the disk thermal structure presented by M. Galloway-Sprietsma et al. (2025) to lower altitudes, particularly in combination with ^{13}CO to better constrain the optical depths.

Several sources in the exoALMA sample show evidence of embedded planets. Comparisons with models suggest that this is likely the case for LkCa 15, J1615, and J1842, with planet masses estimated to range from one to five Jupiter masses. There is also potential kinematic evidence for planets in SY Cha and AA Tau, but reaching a definitive conclusion is more challenging, due either to simplifications in our model for SY Cha, which does not accurately capture the shape of the

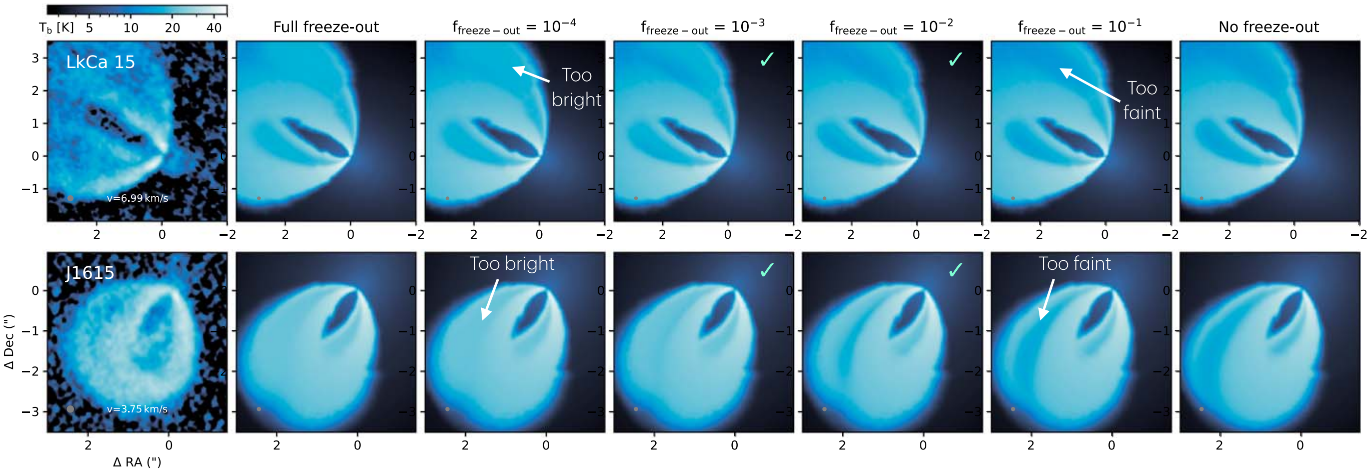

Figure 8. Comparison of ^{12}CO observations of LkCa 15 and J1615 (left column) with synthetic channel maps with various amounts of freeze-out depletion, from full freeze-out (i.e., CO abundance is 0 where the temperature is below 10 K) to no freeze-out (i.e., CO abundance is the same as in the disk surface: 10^{-4}, even where $T < 20$ K). For both sources, we used the best hydrodynamical model from Figure 7. The color map scales with the log of the brightness temperature to highlight the emission from the disk midplane where the models differ. The green checkmarks indicate the models that visually best reproduce the observations.

velocity signature, or to a limited signal-to-noise ratio for AA Tau. We note that while the single-planet model can reproduce the observed velocity kinks, the models are not perfect and do not account for all the detected kinematic structures. This is the case, for instance, in LkCa 15, where additional deviations appear across multiple channels. This is illustrated in Figure 5, where we overlay the expected location of the planet wake (R. R. Rafikov 2002). We use here the same thermal structure as in the phantom model, and project the wake vertically from the midplane onto the emitting surface detected with dynamite. While some substructures align with the wake's location, additional substructures are observed in the data.

One major limitation of our models is the assumption of a vertically isothermal profile in phantom. Comparisons between live radiation and vertically isothermal models showed only minor differences in the kinematic signatures for the Herbig Ae star HD 97048 (C. Pinte et al. 2009), but surface thermal waves (e.g., P. D'Alessio et al. 1999) or buoyancy spirals (J. Bae et al. 2021) are more likely to develop around lower-mass T Tauri stars. Other physical processes can also produce deviations from Keplerian rotation, including magnetorotational instability (MRI), GI, and vertical shear instability (VSI; see, for instance, M. Barraza-Alfaro et al. 2025, for a comparison). The filamentary structures we see in some sources resemble some predictions of VSI or MRI. None of the exoALMA sources seem to display kinematic signatures of GI (C. Hall et al. 2020; C. Longarini et al. 2021). We also note that the interplay between instabilities and planets can also significantly affect the expected kinematic signatures, as shown by S. Rowther et al. (2020) in the case of GI. A more systematic comparison with models would be necessary to determine whether alternative explanations or additional physics (e.g., vertical thermal structures, additional planets, or instabilities) are required to fully match the observations.

We find planet orbital separations between 80 and 310 au, comparable to the 260 au of HD 163296b also detected via disk kinematics (C. Pinte et al. 2018b). The exoALMA sample is biased toward large and bright disks, but our results (six sources with evidence for planets in a sample of 15 sources) indicate that the presence of planets at large separation is not rare if the disk is large enough. By deprojecting the velocity kinks to the midplane (Figure 5), we find that most of the potential planets are located just outside the dust continuum emission (P. Curone et al. 2025), indicating that they may be truncating the dusty disk. For AA Tau, the deprojected kink location falls in the dust continuum gap at 80 au, similar to HD 97048b (C. Pinte et al. 2009) and the planet candidates in the DSHARP sample (C. Pinte et al. 2020). The planet candidates are also outside the detected scattered light (J. de Boer et al. 2016; B. B. Ren et al. 2023; C. Ginski et al. 2024) and do not seem to be directly related to the structures seen in the near-infrared images, except maybe for J1615 where the candidate is located just outside the outer ring.

The complexity of the observed structures, particularly the filaments between surfaces shown in Figure 3, suggests that accurately constraining fine parameters, such as the degree and origin of nonthermal broadening, will likely require a precise representation of the underlying emission from the disk. This is especially intriguing in the case of DM Tau, where nonzero turbulent broadening was inferred from intermediate-resolution ($0\farcs4$) CO observations (K. Flaherty et al. 2020). The exoALMA data for DM Tau show large-scale diffuse emission, striated structures, and nonzero CO emission from the midplane, which may result in line broadening at lower resolution due to smearing. We refer to C. Hardiman et al. (2025, in preparation) for a detailed discussion of nonturbulent broadening in DM Tau.

Despite the improved data quality provided by exoALMA, the low-level kinematic deviations seen in most of the disks—and the potential additional physical processes associated with them—currently set the lower limit for the smallest planet masses we can detect through disk kinematics at $\approx 1\,M_{\rm Jup}$. Deviations caused by lighter planets are of the same order or smaller than this background of deviations, and pushing down our planet detection limit will require more detailed models, for instance accounting for vertical temperature and velocity gradients, self-gravity (e.g., C. Longarini et al. 2025), or collisional broadening (e.g., C. T. Yoshida et al. 2025).

6. Conclusions

We present an in-depth analysis of ^{12}CO channel maps across 15 protoplanetary disks from the exoALMA survey. Our study reveals a variety of complex kinematic structures, highlighting the intricate interplay between gas dynamics, including potential planetary interactions, and disk physics and chemistry. The key findings of this work are summarized as follows.

1. We detect velocity deviations from Keplerian rotation in 13 out of the 15 disks, which manifest in a range of kinematic structures, including extended arcs, spirals, velocity kinks, and filamentary structures.
2. Kinematic signatures observed in six disks point toward the presence of embedded planets. Our preliminary hydrodynamic and radiative transfer simulations suggest that the planets responsible for the observed velocity kinks have masses in the range 1–5 $M_{\rm Jup}$ and orbital distances between 80 and 310 au.
3. Additional physics (e.g., vertical temperature and velocity gradients, multiple planets, or disk instabilities) may be required to fully explain the observed deviations from Keplerian motion. Our models are limited in their ability to place tight constraints on planet masses due to these additional complexities. The background of deviations in the observed velocity fields may hide low-mass embedded planets and currently sets the lower limit for the kinematic detection of planets to $\approx 1\ M_{\rm Jup}$.
4. The complexity and amplitude of some of the observed kinematic structures, particularly in systems such as MWC 758, suggest that more massive bodies or interactions with the surrounding environment (e.g., infall or outflows) are contributing to the observed deviations.
5. The vertical CO snowline is clearly detected in seven disks where the upper and lower emission surfaces are well separated. Our results indicate partial ^{12}CO freeze-out in the midplane, with a depletion factor of $\approx 10^{-3}$–10^{-2} compared to the warm molecular layer. Additionally, we systematically detect desorption signatures in the outer regions of these disks.

Acknowledgments

This Letter makes use of the following ALMA data: ADS/JAO.ALMA#2021.1.01123.L. ALMA is a partnership of ESO (representing its member states), NSF (USA) and NINS (Japan), together with NRC (Canada), MOST and ASIAA (Taiwan), and KASI (Republic of Korea), in cooperation with the Republic of Chile. The Joint ALMA Observatory is operated by ESO, AUI/NRAO and NAOJ. The National Radio Astronomy Observatory is a facility of the National Science Foundation operated under cooperative agreement by Associated Universities, Inc. We thank the North American ALMA Science Center (NAASC) for their generous support including providing computing facilities and financial support for student attendance at workshops and publications. This work was supported by resources awarded under Astronomy Australia Ltd's ASTAC merit allocation scheme on the OzSTAR national facility at Swinburne University of Technology. The OzSTAR program receives funding in part from the Astronomy National Collaborative Research Infrastructure Strategy (NCRIS) allocation provided by the Australian Government, and from the Victorian Higher Education State Investment Fund (VHESIF) provided by the Victorian Government. C.P. acknowledges funding from the Australian Research Council via FT170100040, DP180104235, and DP220103767. J.B. acknowledges support from NASA XRP grant No. 80NSSC23K1312. M.B., D.F., and J.S. have received funding from the European Research Council (ERC) under the European Union's Horizon 2020 research and innovation program (PROTOPLANETS, grant agreement No. 101002188). P.C. acknowledges support by the Italian Ministero dell'Istruzione, Università e Ricerca through the grant Progetti Premiali 2012—iALMA (CUP C52I13000140001) and by the ANID BASAL project FB210003. S.F. is funded by the European Union (ERC, UNVEIL, 101076613) and acknowledges financial contribution from PRIN-MUR 2022YP5ACE. M.F. is supported by a grant-in-Aid from the Japan Society for the Promotion of Science (KAKENHI: No. JP22H01274). J.D.I. acknowledges support from an STFC Ernest Rutherford Fellowship (ST/W004119/1) and a University Academic Fellowship from the University of Leeds. Support for A.F.I. was provided by NASA through the NASA Hubble Fellowship grant No. HST-HF2-51532.001-A awarded by the Space Telescope Science Institute, which is operated by the Association of Universities for Research in Astronomy, Inc., for NASA, under contract NAS5-26555. C.L. has received funding from the European Union's Horizon 2020 research and innovation program under the Marie Sklodowska-Curie grant agreement No. 823823 (DUSTBUSTERS) and by the UK Science and Technology research Council (STFC) via the consolidated grant ST/W000997/1. G.R. acknowledges funding from the Fondazione Cariplo, grant No. 2022-1217, and the European Research Council (ERC) under the European Union's Horizon Europe Research & Innovation Programme under grant agreement No. 101039651 (DiscEvol). F. Menard received funding from the European Research Council (ERC) under the European Union's Horizon Europe research and innovation program (grant agreement No. 101053020, project Dust2Planets). H-.W.Y. acknowledges support from National Science and Technology Council (NSTC) in Taiwan through grant NSTC 113-2112-M-001-035- and from the Academia Sinica Career Development Award (AS-CDA-111-M03). G.W.F. acknowledges support from the European Research Council (ERC) under the European Union Horizon 2020 research and innovation program (grant agreement No. 815559 (MHDiscs)). G.W.F. was granted access to the HPC resources of IDRIS under the allocation A0120402231 made by GENCI. Support for B.Z. was provided by The Brinson Foundation. Views and opinions expressed by ERC-funded scientists are, however, those of the author(s) only and do not necessarily reflect those of the European Union or the European Research Council. Neither the European Union nor the granting authority can be held responsible for them.

Software: casa (Team CASA et al. 2022), casa_cube (C. Pinte 2022a), dynamite (C. Pinte et al. 2018a), phantom (D. J. Price et al. 2018), mcfost (C. Pinte et al. 2006; C. Pinte et al. 2009), pymcfost (C. Pinte 2022b).

ORCID iDs

Christophe Pinte https://orcid.org/0000-0001-5907-5179
John D. Ilee https://orcid.org/0000-0003-1008-1142
Jane Huang https://orcid.org/0000-0001-6947-6072
Myriam Benisty https://orcid.org/0000-0002-7695-7605
Stefano Facchini https://orcid.org/0000-0003-4689-2684
Misato Fukagawa https://orcid.org/0000-0003-1117-9213
Richard Teague https://orcid.org/0000-0003-1534-5186

Jaehan Bae https://orcid.org/0000-0001-7258-770X
Marcelo Barraza-Alfaro https://orcid.org/0000-0001-6378-7873
Gianni Cataldi https://orcid.org/0000-0002-2700-9676
Nicolás Cuello https://orcid.org/0000-0003-3713-8073
Pietro Curone https://orcid.org/0000-0003-2045-2154
Ian Czekala https://orcid.org/0000-0002-1483-8811
Daniele Fasano https://orcid.org/0000-0003-4679-4072
Mario Flock https://orcid.org/0000-0002-9298-3029
Maria Galloway-Sprietsma https://orcid.org/0000-0002-5503-5476
Himanshi Garg https://orcid.org/0000-0002-5910-4598
Cassandra Hall https://orcid.org/0000-0002-8138-0425
Iain Hammond https://orcid.org/0000-0003-1502-4315
Caitlyn Hardiman https://orcid.org/0009-0003-7403-9207
Thomas Hilder https://orcid.org/0000-0001-7641-5235
Andrés F. Izquierdo https://orcid.org/0000-0001-8446-3026
Kazuhiro Kanagawa https://orcid.org/0000-0001-7235-2417
Geoffroy Lesur https://orcid.org/0000-0002-8896-9435
Giuseppe Lodato https://orcid.org/0000-0002-2357-7692
Cristiano Longarini https://orcid.org/0000-0003-4663-0318
Ryan A. Loomis https://orcid.org/0000-0002-8932-1219
Frédéric Masset https://orcid.org/0000-0002-9626-2210
Francois Menard https://orcid.org/0000-0002-1637-7393
Ryuta Orihara https://orcid.org/0000-0003-4039-8933
Daniel J. Price https://orcid.org/0000-0002-4716-4235
Giovanni Rosotti https://orcid.org/0000-0003-4853-5736
Jochen Stadler https://orcid.org/0000-0002-0491-143X
Hsi-Wei Yen https://orcid.org/0000-0003-1412-893X
Gaylor Wafflard-Fernandez https://orcid.org/0000-0002-3468-9577
David J. Wilner https://orcid.org/0000-0003-1526-7587
Andrew J. Winter https://orcid.org/0000-0002-7501-9801
Lisa Wölfer https://orcid.org/0000-0002-7212-2416
Tomohiro C. Yoshida https://orcid.org/0000-0001-8002-8473
Brianna Zawadzki https://orcid.org/0000-0001-9319-1296

References

Allard, F., Homeier, D., & Freytag, B. 2012, RSPTA, 370, 2765
Avenhaus, H., Quanz, S. P., Garufi, A., et al. 2018, ApJ, 863, 44
Bae, J., Flock, M., Izquierdo, A., et al. 2025, ApJL, 984, L12
Bae, J., Teague, R., & Zhu, Z. 2021, ApJ, 912, 56
Ballabio, G., Nealon, R., Alexander, R. D., et al. 2021, MNRAS, 504, 888
Barraza-Alfaro, M., Flock, M., Béthune, W., et al. 2025, ApJL, 984, L21
Benisty, M., Juhasz, A., Boccaletti, A., et al. 2015, A&A, 578, L6
Boehler, Y., Weaver, E., Isella, A., et al. 2017, ApJ, 840, 60
Bollati, F., Lodato, G., Price, D. J., & Pinte, C. 2021, MNRAS, 504, 5444
Bruderer, S., van Dishoeck, E. F., Doty, S. D., & Herczeg, G. J. 2012, A&A, 541, A91
Byrne, P. B. 1986, IrAJ, 17, 294
Calcino, J., Hilder, T., Price, D. J., et al. 2022, ApJL, 929, L25
Calcino, J., Norfolk, B. J., Price, D. J., et al. 2024, MNRAS, 534, 2904
Calcino, J., Price, D. J., Pinte, C., et al. 2023, MNRAS, 523, 5763
Casassus, S., & Pérez, S. 2019, ApJL, 883, L41
Cuello, N., Louvet, F., Mentiplay, D., et al. 2020, MNRAS, 491, 504
Curone, P., Facchini, S., Andrews, S. M., et al. 2025, ApJL, 984, L9
D'Alessio, P., Cantó, J., Hartmann, L., Calvet, N., & Lizano, S. 1999, ApJ, 511, 896
de Boer, J., Salter, G., Benisty, M., et al. 2016, A&A, 595, A114
de Gregorio-Monsalvo, I., Ménard, F., Dent, W., et al. 2013, A&A, 557, A133
Dullemond, C. P., Isella, A., Andrews, S. M., Skobleva, I., & Dzyurkevich, N. 2020, A&A, 633, A137
Flaherty, K., Hughes, A. M., Simon, J. B., et al. 2020, ApJ, 895, 109
Galloway-Sprietsma, M., Bae, J., Izquierdo, A., et al. 2025, ApJL, 984, L10
Gardner, C., Isella, A., Hui, L., et al. 2025, ApJL, 984, L16
Garg, H., Pinte, C., Christiaens, V., et al. 2021, MNRAS, 504, 782
Ginski, C., Garufi, A., Benisty, M., et al. 2024, A&A, 685, A52
Hall, C., Dong, R., Teague, R., et al. 2020, ApJ, 904, 148
Hammond, I., Christiaens, V., Price, D. J., et al. 2022, MNRAS, 515, 6109
Hilder, T., Casey, A. R., Price, D. J., et al. 2025, ApJL, 984, L13
Izquierdo, A. F., Stadler, J., Bae, J., et al. 2025, ApJL, 984, L8
Law, C. J., Crystian, S., Teague, R., et al. 2022, ApJ, 932, 114
Law, C. J., Teague, R., Loomis, R. A., et al. 2021, ApJS, 257, 4
Lodato, G., Rampinelli, L., Viscardi, E., et al. 2023, MNRAS, 518, 4481
Longarini, C., Lodato, G., Rosotti, G., et al. 2025, ApJL, 984, L17
Longarini, C., Lodato, G., Toci, C., et al. 2021, ApJL, 920, L41
Loomis, R., Facchini, S., Benisty, M., et al. 2025, ApJL, 984, L7
Martinez-Brunner, R., Casassus, S., Pérez, S., et al. 2022, MNRAS, 510, 1248
Muto, T., Grady, C. A., Hashimoto, J., et al. 2012, ApJL, 748, L22
Norfolk, B. J., Pinte, C., Calcino, J., et al. 2022, ApJL, 936, L4
Öberg, K. I., Facchini, S., & Anderson, D. E. 2023, ARA&A, 61, 287
Paneque-Carreño, T., Miotello, A., van Dishoeck, E. F., et al. 2023, A&A, 669, A126
Pérez, L. M., Benisty, M., Andrews, S. M., et al. 2018, ApJL, 869, L50
Pinte, C. 2022a, casa cube: Display and Analyze Astronomical Data Cubes, Astrophysics Source Code Library, ascl:2207.025
Pinte, C. 2022b, pymcfost: Python Interface to the MCFOST 3D Radiative Transfer Code, Astrophysics Source Code Library, ascl:2207.024
Pinte, C. 2025, exoALMA X. Data Products, v1, Harvard Dataverse doi:10.7910/DVN/H5QUQT
Pinte, C., Hammond, I., Price, D. J., et al. 2023b, MNRAS, 526, L41
Pinte, C., Harries, T. J., Min, M., et al. 2009, A&A, 498, 967
Pinte, C., Ménard, F., Duchêne, G., & Bastien, P. 2006, A&A, 459, 797
Pinte, C., Ménard, F., Duchêne, G., et al. 2018a, A&A, 609, A47
Pinte, C., Price, D. J., Ménard, F., et al. 2018b, ApJL, 860, L13
Pinte, C., Price, D. J., Ménard, F., et al. 2020, ApJL, 890, L9
Pinte, C., Teague, R., Flaherty, K., et al. 2023a, in ASP Conf. Ser. 534, Protostars and Planets VII, ed. S. Inutsuka et al. (San Francisco, CA: ASP)
Pinte, C., van der Plas, G., Ménard, F., et al. 2019, NatAs, 3, 1109
Price, D. J., Wurster, J., Tricco, T. S., et al. 2018, PASA, 35, e031
Qi, C., & Wilner, D. J. 2024, ApJ, 977, 60
Rafikov, R. R. 2002, ApJ, 569, 997
Ragusa, E., Lynch, E., Laibe, G., Longarini, C., & Ceppi, S. 2024, A&A, 686, A264
Reggiani, M., Christiaens, V., Absil, O., et al. 2018, A&A, 611, A74
Ren, B. B., Benisty, M., Ginski, C., et al. 2023, A&A, 680, A114
Rosenfeld, K. A., Andrews, S. M., Hughes, A. M., Wilner, D. J., & Qi, C. 2013, ApJ, 774, 16
Rowther, S., Meru, F., Kennedy, G. M., Nealon, R., & Pinte, C. 2020, ApJL, 904, L18
Siess, L., Dufour, E., & Forestini, M. 2000, A&A, 358, 593
Stadler, J., Benisty, M., Izquierdo, A., et al. 2023, A&A, 670, L1
Stadler, J., Benisty, M., Winter, A. J., et al. 2025, ApJL, 984, L11
Stempels, H. C., & Gahm, G. F. 2004, A&A, 421, 1159
Teague, R., Bae, J., Aikawa, Y., et al. 2021, ApJS, 257, 18
Teague, R., Benisty, M., Facchini, S., et al. 2025, ApJL, 984, L6
Team CASA, Bean, B., Bhatnagar, S., et al. 2022, PASP, 134, 114501
Verrios, H. J., Price, D. J., Pinte, C., Hilder, T., & Calcino, J. 2022, ApJL, 934, L11
Weingartner, J. C., & Draine, B. T. 2001, ApJ, 548, 296
Woitke, P., Kamp, I., & Thi, W. F. 2009, A&A, 501, 383
Yoshida, C. T., Curone, P., Stadler, J., et al. 2025, ApJL, 984, L19
Zawadzki, B., Czekala, I., Galloway-Sprietsma, M., et al. 2025, ApJL, 984, L14